Fractal dimension of velocity signals in high-Reynolds-number hydrodynamic turbulence

Alberto Scotti and Charles Meneveau
Department of Mechanical Engineering, The Johns Hopkins University, Baltimore, Maryland 21218

Seyed G. Saddoughi
Center for Turbulence Research, Stanford University, Stanford, California 94305-3030
(Received 15 December 1994)

In this paper the fractal nature of velocity signals as measured in turbulent flows is investigated. In particular, we study the geometrical nature of the graph $(x,f(x))$ of the function f that gives one component of the velocity at position x. Special emphasis is given to the effects that a limited resolution of the signal, or natural small-scale cutoffs, have on the estimate of the fractal dimension, and a procedure to account for such finite-size effects is proposed and tested on artificial fractal graphs. We then consider experimental data from three turbulent flows: the wake behind a circular cylinder, the atmospheric surface layer, and the rough-wall zero-pressure-gradient boundary layer developing on the test-section ceiling of the 80×120 ft^2 full-scale NASA Ames wind tunnel (the world's largest wind tunnel). The results clearly indicate that at high Reynolds numbers, turbulent velocity signals have a fractal dimension of $D\simeq 1.7\pm 0.05$, very near the value of $D=\frac{5}{3}$ expected for Gaussian processes with a $-\frac{5}{3}$ power law in their power spectrum.

PACS number(s): 47.27.−i, 47.53.+m

I. INTRODUCTION

Most of the applications of fractals to turbulence have so far been devoted to the study of subsets of the region occupied by turbulent flow where a given property is satisfied. For example, isoconcentration surfaces of advected variables and interfaces, or the structure of spatial distribution of dissipation rates, have been characterized as fractals or multifractals and the appropriate dimensions have been measured (see Refs. [1–7]). The main goal of this paper is to establish to what extent it is possible to treat signals representing any of the three turbulent velocity components as self-affine fractal. Figure 1 shows a times series of the streamwise velocity component measured in the atmospheric boundary layer (details will be given later). Using Taylor's hypothesis, such a signal can be regarded as a spatial one-dimensional "cut" through a frozen three-dimensional field. We are led to believe that the fractal dimension of the velocity profile $u(x)$ is not an integer mainly because of the well-known power-law decay of the energy spectrum in the inertial range [8,9]. For such a signal, the second-order structure function is itself a power law and we have

$$\langle \hat{u}(k)\hat{u}^*(k)\rangle \sim k^{-\alpha} \Longleftrightarrow \langle |u(x+r)-u(x)|^2\rangle \sim r^{\alpha-1} . \quad (1)$$

It has been proven [10] that for processes with multipoint Gaussian statistics Eq. (1) implies that the fractal dimension of almost all realizations of such a random signal is given by

$$d_f=\frac{5-\alpha}{2} . \quad (2)$$

Therefore, for a turbulent velocity signal at high Reynolds number one might expect to find a fractal dimension equal to $\frac{5}{3}\simeq 1.66$. Yet it is well known that the multipoint statistic for a turbulent flow is not Gaussian [9], so that it becomes necessary to establish whether the derivation from Gaussianity affects the fractal nature and the value of the dimension (see Ref. [11] for some related numerical experiments). For this purpose, in this paper the fractal dimension of velocity signals in a variety of turbulent flows is measured, mostly using the well-known box-counting method [12] but at times complementing it with the variational method [13]. In Ref. [14], similar techniques have been applied to fractional Brownian motion and to turbulent signals, with special emphasis on the dimension of level sets. For the turbulent signals the fractal dimensions found were consistent with $d_f=\frac{5}{3}$.

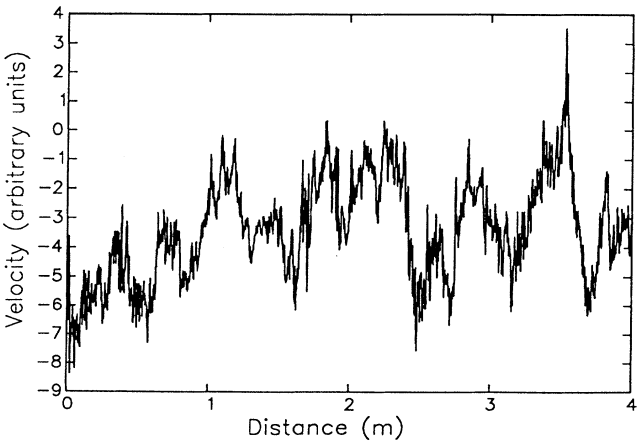

FIG. 1. Typical turbulent signal of streamwise velocity measured by a hot-wire anemometer in the atmospheric surface layer, using Taylor's frozen flow hypothesis.

For level sets the situation became less clear, as scaling ranges and dimension appear to depend on the threshold. Level sets of turbulent velocity signals were also considered in Ref. [15].

In the present paper we focus attention on the signal and not on level sets and we analyze in detail how small-scale cutoffs affect the power-law behavior. To gain confidence in the results, stringent tests of power-law detection are applied. This leads to the conclusion that pure power-law behavior is absent in all but the highest Reynolds number data set analyzed, essentially because of finite-size corrections to scaling. The same effects are observed during analysis of synthetic fractal functions with known dimension but finite cutoff scale. A functional form for these scaling corrections is proposed, which can be used to both check for fractality and to measure the dimension. This procedure is applied to some synthetic fractals and then to the experimental data sets.

Section II reviews some traditional schemes for obtaining numerically the fractal dimension of signals, while Sec. III applies these to synthetic graphs of known dimension. The results are analyzed in Sec. IV, where a procedure for taking scaling corrections explicitly into account during data analysis is proposed. Section V gives a description of the turbulence data sets and Sec. VI presents the main results of the analysis of the experimental data. A summary and conclusions are given in Sec. VII.

II. NUMERICAL SCHEMES FOR THE COMPUTATION OF THE FRACTAL DIMENSION OF GRAPHS

Several numerical schemes have been devised to compute the fractal dimension of time series or graphs (see Refs. [16] and [13]). The simplest consists in a straightforward application of the definition of box-counting dimension: one covers the graph with a grid of rectangles $\varepsilon \times \theta\varepsilon$ in size, where θ is an arbitrary aspect ratio. Then one counts the number $N(\varepsilon)$ of rectangles that contain a portion of the graph [see Fig. 2(a)]. The dimension is then defined as

$$d_f = \lim_{\varepsilon \to 0} \frac{\log N(\varepsilon)}{\log \varepsilon} \ . \tag{3}$$

Although this method is not completely free from defects, especially at large scales where the discrete nature of the boxes can lead to fluctuations, box counting has the advantage of being conceptually simple, easy to code and discuss. As an example of other methods that can be used, we mention the so-called "variational method" [13], which has recently gained popularity. Instead of counting the number of boxes required to cover the graph, one measures the area of the envelope that contains the graph [see Fig. 2(b)], this envelope being defined on scale ε as

$$v(x,\varepsilon) = \sup_{x' \in B(x,\varepsilon)} f(x') - \inf_{x' \in B(x,\varepsilon)} f(x') \ , \tag{4}$$

$$B(x,\varepsilon) = \{x'' \in [a,b]: \ |x - x''| < \varepsilon\} \ . \tag{5}$$

The area is given by

$$\mathcal{V}(\varepsilon) = \int_a^b v(x,\varepsilon)\, dx \ . \tag{6}$$

The fractal dimension can be obtained by

$$d_f = \lim_{\varepsilon \to 0} \left[2 - \frac{\log \mathcal{V}(\varepsilon)}{\log \varepsilon} \right] \ . \tag{7}$$

Since $\mathcal{V}(\varepsilon)$ is continuous, it typically exhibits fewer fluctuations at large scales than the box-counting method. A disadvantage of the box-counting algorithm for analysis of self-affine sets is that the aspect ratio θ must be properly selected. It is known (see Refs. [17,18]) that if θ is so large as to imply rectangular boxes that are of a height comparable to the range of the function, the box dimension may tend to 1. However, if θ is chosen such that even at large ε one needs several boxes to cover the graph's vertical extent, box counting will yield the correct dimension. Thus we will make use mainly of box counting (using very small θ), resorting to the variational method when the former is spoiled by fluctuations, and for consistency checks.

Local fractal dimension

Regardless of the method employed, the fractal dimension is always associated with the exponent of a power

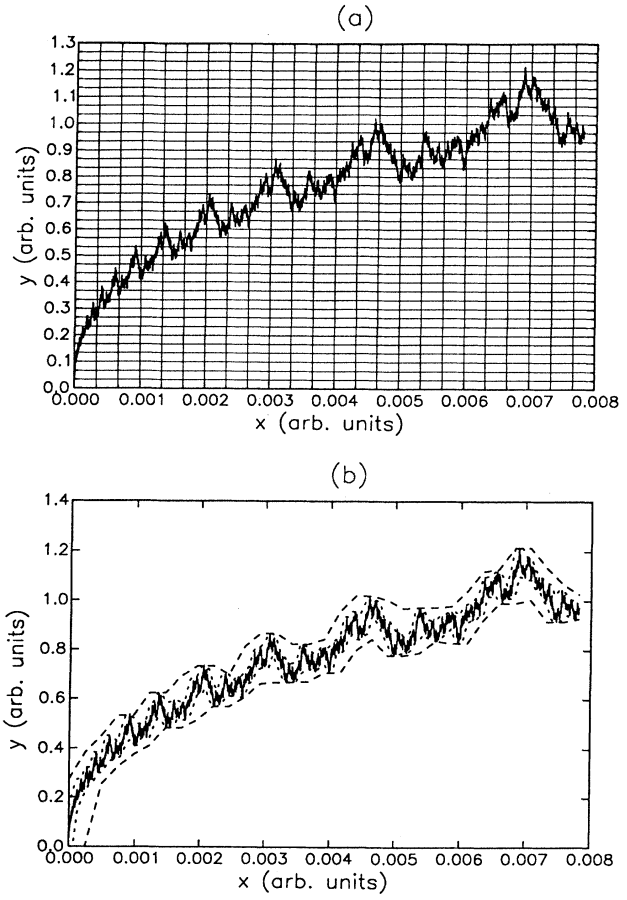

FIG. 2. Covering a signal using (a) rectangles for the box counting method or (b) the "variation sausage" for the method of Dubuc *et al.* [13].

law, that is to say, there exists a quantity $N_{\pm}(\varepsilon)$ (number of boxes, area of the envelope, etc.) such that $N_{\pm}(\varepsilon) \sim \varepsilon^{\pm d_f}$. For a number of reasons it is not advisable to compute d_f explicitly from its definition—at small scales $N_{\pm}(\varepsilon)$ can be affected by sizable errors and also, since $N_{\pm}(\varepsilon) \simeq C\varepsilon^{\pm d_f}$ in general, the limit converges very slowly [as $(\log\varepsilon)^{-1}$]. Hence, traditionally d_f has been evaluated by plotting $\log N(\varepsilon)$ vs $\log\varepsilon$ and measuring the slope of the best linear fit. Recently, some arguments have been made that such an approach can be misleading [7,19]. Praskovsky *et al.* in Ref. [7] show with a counterexample that what may seem like a straight line in a log-log plot can actually be far from a true power law. Following these references we consider taking the logarithmic derivative

$$d_f(\varepsilon) = \pm \frac{d \log N_{\pm}(\varepsilon)}{d \log \varepsilon} . \tag{8}$$

We refer to $d_f(\varepsilon)$ as the *local* dimension (local in scale), as opposed to d_f, which we may call *global*. For a fractal set, $d_f(\varepsilon)$ has to tend to a (noninteger) constant at small ε. For a fractal arising in the real world, there are necessarily cutoff scales below which the scaling changes. In addition, if a signal is discretely sampled at a finite rate, an "artificial" cutoff scale may be introduced. Mandelbrot calls these objects "prefractals" [20]. Again, the common belief is that $d_f(\varepsilon)$ should remain constant over a range of scales somewhere above this cutoff scale. To test these ideas, we consider synthetic prefractals, generated in different ways, with known fractal dimension.

III. LOCAL DIMENSION OF SYNTHETIC PREFRACTAL GRAPHS

A. Weierstrass functions

Let g: $[0,1] \to \mathbb{C}$ be a complex function defined as

$$g(x) = \sum_{n=-\infty}^{\infty} \frac{(1 - e^{ib^n x}) e^{i\phi_n}}{b^{(2-d)n}} , \quad 1 < d < 2, \ \phi_n \in [0, 2\pi] . \tag{9}$$

This is the Weierstrass function, originally introduced by Weierstrass as an example of a continuous but nowhere differentiable function. The graphs of both the real and the imaginary part are fractal, with box dimension d [at the time of this writing, it is apparently not known in the literature whether the Hausdorff dimension coincides with d or is smaller (see [21] for more details)]. An interesting case occurs if all the phases ϕ_n are set to zero. Then the function has the exact scaling property

$$g(bx) = b^{2-d} g(x) . \tag{10}$$

As will be seen later, this feature makes $g(x)$ an excellent test case to understand the influence of the sampling frequency on the measured local fractal dimension. Next, we present the results concerning the approximated Weierstrass function

$$g_1(x_i) = \sum_{n=-50}^{50} \frac{1 - \cos(b^n x_i)}{b^{(2-d_f)n}} ,$$

$$d_f = 1.6, b = 2.0, x_i = i\Delta x, \ i = 1, \ldots, 1/\Delta x . \tag{11}$$

As Fig. 3(a) shows, besides depending on ε, the resulting local dimension strongly depends on the number of sampling points (here we have used $\Delta x = 2^{-10}$, 2^{-12}, 2^{-16}, and 2^{-19}). Unresolving small scales affects the result on scales that are larger than the smallest resolved scale (proportional to the inverse of the sampling frequency). We can understand this if we consider Fig. 3(b), where we have plotted a portion of the Weierstrass function sampled at different levels of resolution: unresolving the small scales leads to an underestimation of the total variation of the function over some region and therefore to an underestimation of the number of boxes needed to cover the signal (this result is similar to the one discussed in Yordanov and Nickolaev [22] for random time series). Also note that at large scales box counting tends to underestimate the local dimension, almost independent of the sampling frequency.

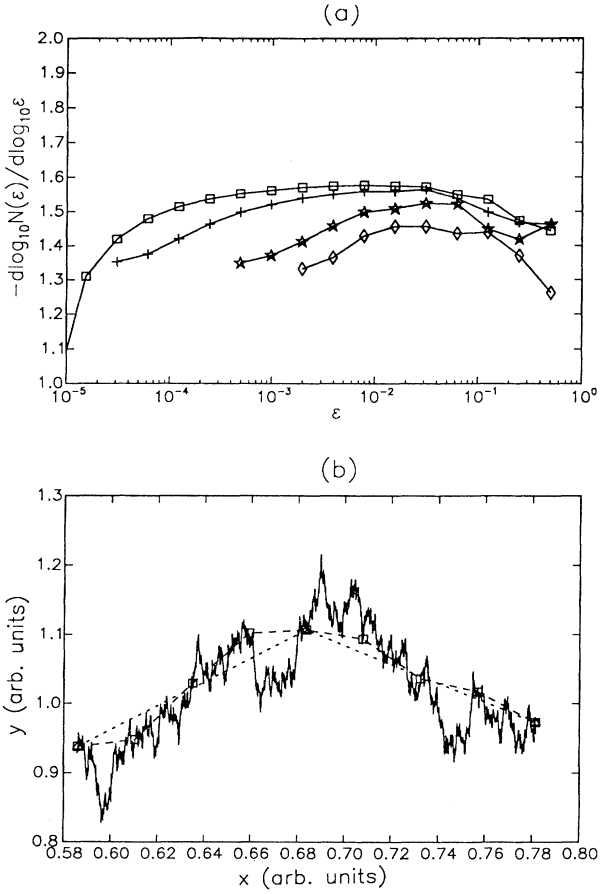

FIG. 3. (a) Local fractal dimension of the Weierstrass function sampled at different levels of resolution $\Delta x = 2^{-10}$, 2^{-12}, 2^{-16}, and 2^{-19} (diamonds, stars, crosses, and squares, respectively). (b) Weierstrass function plotted at different levels of resolution (solid line, $\Delta x = 2^{-19}$; dashed line, $\Delta x = 2^{-12}$, dotted line, $\Delta x = 2^{-10}$).

B. Graph generated by fractal interpolation

Another method to generate graphs with fractal dimension $d_f > 1$ is to apply the fractal interpolation technique (FIT) to a set of points [23,24]. Given $n+1$ pairs in the real plane (x_i, y_i), $i=0, \ldots, n$, $a=x_0 < \cdots < x_n = b$, the FIT produces the graph of a continuous function $f: [a,b] \to \mathbb{R}$, $y_i = f(x_i)$, with a prescribed fractal dimension. The FIT introduces n affine transformations of the real plane into itself $w_i: \mathbb{R}^2 \to \mathbb{R}^2$, each depending on a parameter $-1 < d_i < 1$; the graph is defined as the fixed point of the transformation $W = \bigcup_{i=1}^{n} w_i$. The fractal dimension is given by solving

$$\sum_{i=0}^{n} |d_i| \left[\frac{x_i - x_{i-1}}{x_n - x_0} \right]^{d_f - 1} = 1 , \tag{12}$$

provided $\sum_i |d_i| > 1$. The process that generates the graph is similar to a multiplicative one. One starts with a piecewise linear interpolation and then proceeds to replicate the graph on smaller and smaller intervals by means of affine transformations that contract by a factor d_i in the y direction.

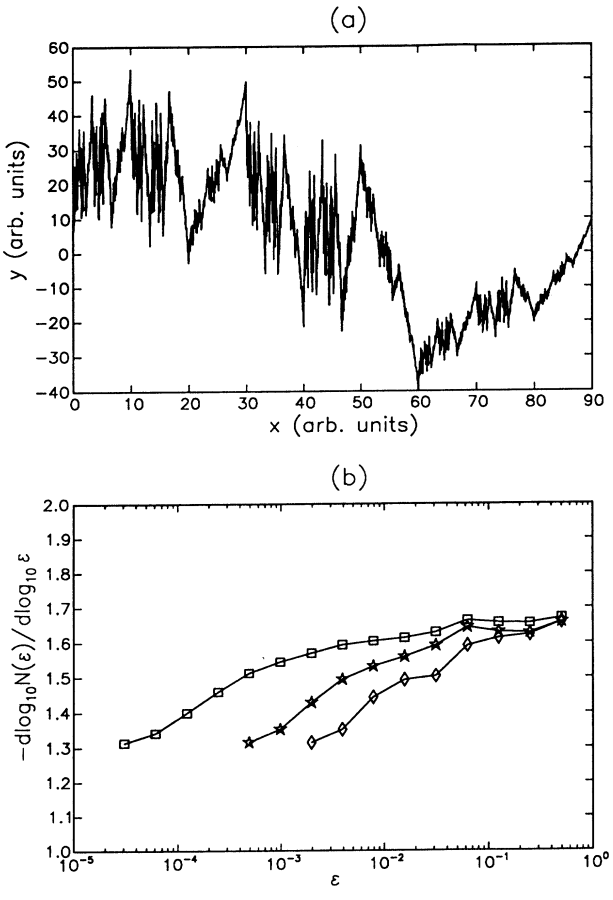

FIG. 4. (a) Signal obtained by fractal interpolation. (b) Local fractal dimension of the FIT function samples at different levels of resolution $\Delta x = 2^{-10}$, 2^{-12}, and 2^{-16} (diamonds, stars, and squares, respectively).

With this technique it is possible to generate very quickly signals with high resolution. We have chosen to interpolate between four points selected randomly. The vertical scaling factors were chosen to be different ($d_1 = 0.8, d_2 = 0.9$, and $d_3 = 0.3$). The resulting fractal dimension is $d_f = 1.63$ [Fig. 4(a)]. We have used three different sampling frequencies $\Delta x^{-1} = 2^{10}$, 2^{12}, and 2^{16}. In this case too, as Fig. 4(b) shows, the local fractal dimension depends on the sampling frequency. From these results it is apparent that if the local slope of the log-log plot is to be used to test for fractal behavior and for finding the true dimension, one would need at least $\Delta x \sim 2^{-16}$. This is an enormous scale-ratio not often encountered in physical experimental data. It is then necessary to understand the origin of the deviations from $d_f(\varepsilon) = d_f$ at small scales and how these depend on the small-scale cutoff.

IV. ANALYSIS

A modified power-law form for the scaling of measured number of boxes consistent with the preceding results can be

$$N_m(\varepsilon) \sim \varepsilon^{-d_f} f(\varepsilon, \Delta x) , \tag{13}$$

i.e., $N_m(\varepsilon)$ is the product of two factors: ε^{-d_f} (called the leading scaling) and a function f that encompasses the observed corrections. In this section we relate the deviation from pure power-law behavior to the smoothing of the signal at small scales caused either by filtering and discrete sampling or by the natural occurrence of a cutoff scale (prefractals). Thus we call f, defined in Eq. (13), the scaling correction. It accounts for the fact that on scales close to the smallest resolved scale the graph of any fractal looks smoother than what it actually should be [see Fig. 3(b)].

A. Accuracy of variation

In order to illustrate the effect of sampling frequency on the accuracy of box counting, we employ the approximated (prefractal) Weierstrass function $g_1(x)$ introduced in Sec. III A. To fix the notation, let $I_\varepsilon(x_i, \Delta x) = \{x \in [x_i - \varepsilon/2, x_i + \varepsilon/2]: \; x = x_i - \varepsilon/2 + i\Delta x, \; i \in \{1, \ldots, p\}, p = \varepsilon/\Delta x\}$, i.e., $I_\varepsilon(x_i, \Delta x)$ is the subset of the interval $[x_i - \varepsilon/2, x_i + \varepsilon/2]$ that consists of the $p = \varepsilon/\Delta x$ sampling points, where Δx^{-1} is the sampling frequency. Box counting evaluates $V(x_i, \varepsilon, \Delta x) = \sup_{x,y \in I_\varepsilon(x_i, \Delta x)} |g_1(x) - g_1(y)|$ in order to get

$$N(x_i, \varepsilon) \simeq \frac{V(x_i, \varepsilon, \Delta x)}{\theta \varepsilon} , \tag{14}$$

where again θ is a constant factor that depends on the choice of the unit of measure used to express $g_1(x)$. The total number is obtained by summing the contributions from all the points x_i. We are concerned about the accuracy that can be achieved in measuring the total variation $V(x_i, \varepsilon, \Delta x)$ at scale ε when the signal has a cutoff on scale Δx. The accuracy is defined naturally as

$$a(x_i, \varepsilon) = \lim_{\Delta x_{\min} \to 0} \frac{|V(x_i, \varepsilon, \Delta x_{\min}) - V(x_i, \varepsilon, \Delta x)|}{V(x_i, \varepsilon, \Delta x_{\min})} . \tag{15}$$

Yet in practice, we only have $V(x_i,\varepsilon,\Delta x_{\min})$ available, where $\Delta x_{\min}$ is the nonzero spatial resolution of the sampling points. (In our numerical experiment $\Delta x_{\min}=2^{-19}$.) We can overcome this limitation in the following way. For the zero-phase Weierstrass function we know that $g_1(x)\sim 2^{d_f-2}g_1(2x)$. The equality is exact for the Weierstrass function with infinitely many terms, but here we add only 100 terms. The error is very small because the transformation shifts all the terms in the sum one position to the left. This implies that $V(0,\varepsilon,0)\sim 2^{d_f-2}V(0,2\varepsilon,0)$, i.e., an interval of length 2ε sampled at frequency Δx^{-1} is equivalent to an interval of half the length, but sampled at a frequency twice as large. On the other hand, the definition of accuracy is essentially unaffected by the rescaling, because it is a ratio. Also, it is reasonable to assume that $a(x_i,\varepsilon)$ depends weakly on x_i so that the accuracy calculated near the origin reflects the order of magnitude of the accuracy calculated at any other point. Therefore the limit $\Delta x_{\min}\to 0$ can be substituted by the limit $\varepsilon\to\infty$ in Eq. (15).

With the aid of this method we have plotted the sampling frequency $\Delta x^{-1}(a,\Delta x_{\min})$ required to have $a<10\%$ and $a<1\%$ for a segment of length 1 known with a resolution $\Delta x_{\min}$ (Fig. 5). We see that in the region where $\Delta x_{\min}^{-1}$ is less than a critical value, $\Delta x^{-1}(a,\Delta x_{\min})$ grows almost linearly, showing that the sampling frequency is not high enough to reveal all the relevant features. When the critical value is reached at the beginning of the plateau, we are at the point at which the fluctuations below the cutoff scale contribute to the total variation less than the prescribed accuracy. Self-similarity allows us to conclude that the ratio $\varepsilon/\Delta x$ must be larger than a critical value, to estimate the variation with a given accuracy, and this ratio depends on the accuracy and the fractal dimension (in our numerical experiment, with $b=2, d_f=1.6$, and $a=0.01$, this value is ~ 1000). This result indicates that, qualitatively, one needs to consider data with very large separation between scales to obtain a realistic estimate for $N(\varepsilon)$. Yet this is not always possible, whence there is a need to account for the scaling correction in a quantitative fashion.

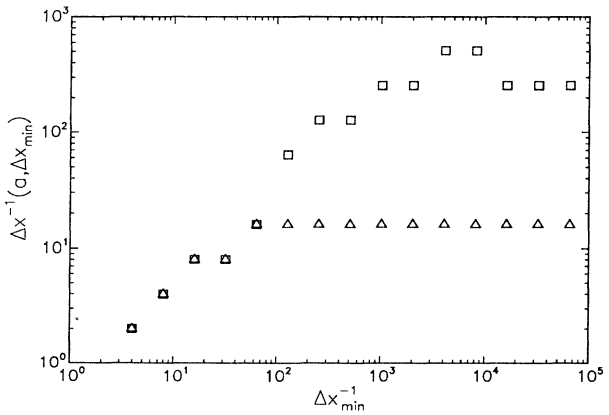

FIG. 5. Logarithm of the minimum resolution (Δx^{-1}) needed for a given accuracy a as a function of the sampling frequency $\Delta x_{\min}^{-1}$ for the Weierstrass function. Squares, $a=1\%$; triangles, $a=10\%$.

B. Scaling correction

The goal is to predict the form of f defined from Eq. (13) as

$$f(\varepsilon,\Delta x)=\varepsilon^{d_f}N_m(\varepsilon)\ . \tag{16}$$

Qualitatively, f should tend to one for large values of ε or for small values of Δx. Since for the Weierstrass function we know what the leading scaling is, we have computed f from the measured $N_m(\varepsilon)$. The results are plotted in Fig. 6(a) for both the Weierstrass and the FIT function (semi-log plots). As can be observed, f appears to collapse when plotted as function of $\varepsilon/\Delta x$. We also see that as $\varepsilon\to\Delta x$, $f(\varepsilon,\Delta x)$ approaches a linear function of

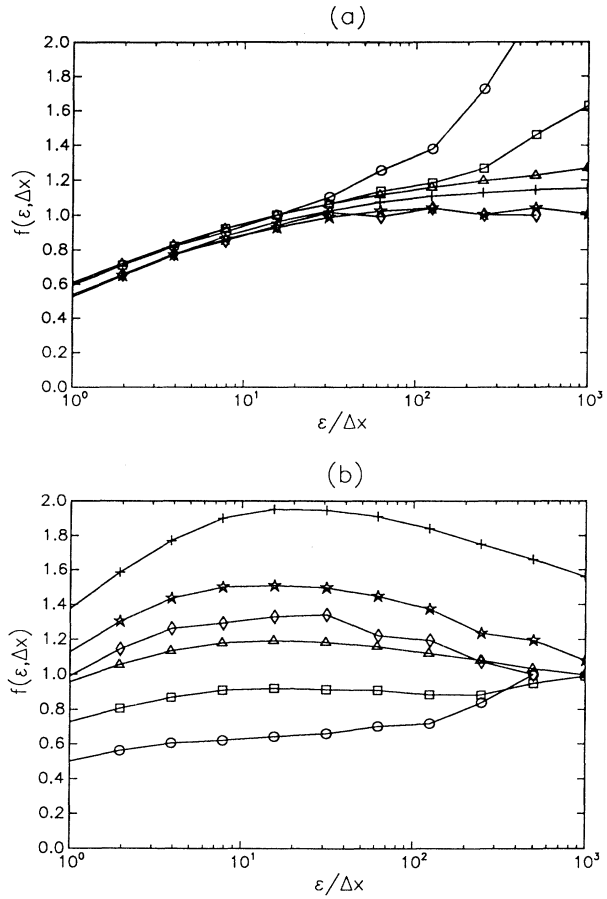

FIG. 6. Small-scale limit of the scaling correction for the Weierstrass and the FIT function. Circles, squares, and triangles are for the Weierstrass function, for sampling resolutions of $\Delta x=2^{-10}$, 2^{-12}, and 2^{-16}, respectively. Diamonds, stars, and crosses are for the fractal interpolation function for resolutions of $\Delta x=2^{-10}$, 2^{-12}, and 2^{-16}, respectively. (a) Scaling correction $f(\varepsilon,\Delta x)$ vs $\varepsilon/\Delta x$ calculated with the true leading exponent for the Weierstrass function ($d_f=1.6$) and for the FIT ($d_f=1.63$). (b) Same as (a) but with a smaller leading exponent $d_f=1.5$.

$\log(\varepsilon/\Delta x)$. In order to show that both the universal shape and the log-linear dependence on $\varepsilon/\Delta x$ is lost if the incorrect value of d_f is used for the leading scaling, in Fig. 6(b) we plot f computed with the leading scaling given by $d_f=1.5$. Clearly the collapse disappears.

To find an expression for f we proceed as follows. Let $N_m^i(\varepsilon)$ be the number of boxes of side ε in a column required to cover the graph at x_i and let $I_\varepsilon(x_i,\Delta x)$ be, as before, the subset of the interval $[x_i-\varepsilon/2,x_i+\varepsilon/2]$ covered by a sampling frequency Δx^{-1}. This number is computed as

$$N_m^i(\varepsilon)\simeq\frac{\sup_{x\in I_\varepsilon(x_i,\Delta x)}g(x)-\inf_{x\in I_\varepsilon(x_i,\Delta x)}g(x)}{\theta\varepsilon}\ , \tag{17}$$

where θ is the unit of measure chosen for the vertical axis. The real Weierstrass function, as well as any self-affine signal, satisfies at all scales the bound

$$|g(x)-g(y)|\le c\,|x-y|^{2-d_f}\ , \tag{18}$$

where c is some constant. Therefore, $c\Delta x^{2-d_f}$ is the order of magnitude of the fluctuations that we cannot see, if we sample the function at scale Δx. Hence the observed variation is related to the "ideal" one by the relation

$$\sup_{x\in I_\varepsilon(x_i,0)}g(x)-\inf_{x\in I_\varepsilon(x_i,0)}g(x)$$
$$=\sup_{x\in I_\varepsilon(x_i,\Delta x)}g(x)-\inf_{x\in I_\varepsilon(x_i,\Delta x)}g(x)+\beta_i c\Delta x^{2-d_f}\ , \tag{19}$$

where $0<\beta_i=o(1)$ is a fluctuating function. This estimate is the crucial ingredient of the results to follow. From Eq. (19) it follows that on scale ε, the measured number of boxes can be expressed as

$$N_m^i(\varepsilon)\simeq\frac{c}{\theta}\left[\varepsilon^{1-d_f}-\beta_i\frac{\Delta x^{2-d_f}}{\varepsilon}\right]$$
$$=\frac{c}{\theta}\varepsilon^{1-d_f}\left[1-\beta_i\left[\frac{\Delta x}{\varepsilon}\right]^{2-d_f}\right]\ . \tag{20}$$

The total number of boxes measured is

$$N_m(\varepsilon)=\sum_{i=1}^{[1/\varepsilon]}N_m^i(\varepsilon)$$
$$\simeq\frac{c}{\theta}\varepsilon^{-d_f}\left[1-\langle\beta_i\rangle\left[\frac{\Delta x}{\varepsilon}\right]^{2-d_f}\right]$$
$$=\varepsilon^{-d_f}f(\varepsilon/\Delta x)\ . \tag{21}$$

The averaging of the β_i's over all $[1/\varepsilon]$ columns of boxes yields $\langle\beta_i\rangle$, which is expected to be $o(1)$. This discussion applies to all the methods that use the quantity on the right-hand side of Eq. (19) to compute the dimension. Therefore, we expect a scaling correction of the same kind for the variational method [see Eq. (4)].

C. Limiting behavior of scaling correction

If $(2-d_f)<1$ and ε is close to Δx we recover the log-linear behavior observed in Fig. 6(a):

$$N_m(\varepsilon)\simeq\frac{c}{\theta}\varepsilon^{-d_f}\left[1-\langle\beta_i\rangle+\langle\beta_i\rangle(2-d_f)\log\frac{\varepsilon}{\Delta x}\right]$$
$$=\gamma\varepsilon^{-d_f}\left[\log\frac{\varepsilon}{\Delta x}+\eta\right]\ , \tag{22}$$

where

$$\eta=\frac{1-\langle\beta_i\rangle}{\langle\beta_i\rangle(2-d_f)}\ ,$$
$$\gamma=\frac{c}{\theta}\langle\beta_i\rangle(2-d_f)\ .$$

This is consistent with the results of Fig. 6, if the "correct" value of d_f is used. Unfortunately, Eq. (22) cannot be used by itself to calculate $(2-d_f)$ unambiguously, because we have no precise estimate of $\langle\beta_i\rangle$ and c.

However, we can extract more information from Eq. (21). Taking the logarithm of $N_m(\varepsilon)$ we have

$$\log N_m(\varepsilon)=\log\frac{c}{\theta}-d_f\log\varepsilon$$
$$+\log\left[1-\langle\beta\rangle\left[\frac{\Delta x}{\varepsilon}\right]^{2-d_f}\right]$$
$$\simeq\log\frac{c}{\theta}-d_f\log\varepsilon$$
$$-\langle\beta_i\rangle e^{(d_f-2)\log(\varepsilon/\Delta x)}\ , \tag{23}$$

valid for $\varepsilon\gg\Delta x$. Hence the local fractal dimension reads

$$d_f(\varepsilon)=\frac{d\log N_m(\varepsilon)}{d\log\frac{1}{\varepsilon}}$$
$$\simeq d_f-\langle\beta_i\rangle(2-d_f)e^{(d_f-2)\log(\varepsilon/\Delta x)}\ . \tag{24}$$

The result is that $d_f(\varepsilon)$ as a function of $\log(\varepsilon/\Delta x)$ approaches the asymptotic value d_f exponentially from below, but with very slow "half time" of order $(2-d_f)^{-1}$. Now, however, we can actually calculate this half time from our data, by examining the logarithm of $[d_f-d_f(\varepsilon)]$. If Eq. (24) holds, $\log[d_f-d_f(\varepsilon)]$ as a function of $\log(\varepsilon/\Delta x)$ should be a straight line of slope (d_f-2). We note that the same analysis applies to the graph generated by the FIT. The numerical experiments agree with this analysis, as shown in Fig. 7. The dotted line represents a perfect exponential approach with the correct value of the half time.

D. From local to global dimension

The results of the numerical experiments show that small-scale cutoffs can be a considerable source of error if fractality and the value of the dimension are to be established with accuracy. Since, as well be seen in Sec. V, all the experimental data to be considered are affected by

this feature, it needs to be considered carefully. So far we have been mostly concerned with the local fractal dimension $d_f(\varepsilon)$. However, it is the fractal dimension d_f that we want to measure, thus we need a way to calculate d_f based on information we have about the local behavior. A first way is to follow the traditional approach (see, e.g., [12,20]) and assume as the fractal dimension the value of the slope of the line that best fits $N_m(\varepsilon)$, possibly discarding some values at the edges. However, as already pointed out, ambiguities in choosing the scaling range and "curving" in the log-log plots often complicate this approach. Alternatively, we can look instead if there is a range of scales where $d_f(\varepsilon)$ remains constant and take that value as the fractal dimension. However, we would then have to conclude that even artificially constructed fractals are not fractals, as, e.g., the measured dimension of the Weierstrass function $g(x)$ depends on external factors, such as the sampling frequency. Dubuc *et al.* [13] suggest to interpolate only the points within a range window, scanning the whole range and retaining the value of the slope that has, say, the best correlation coefficient (the local fractal dimension is then equivalent to the slope of the best fitting when the window includes only three points). They also seem to be aware of the problem represented by undersampling, especially when $d_f > 1.5$, but do not discuss any further the implications.

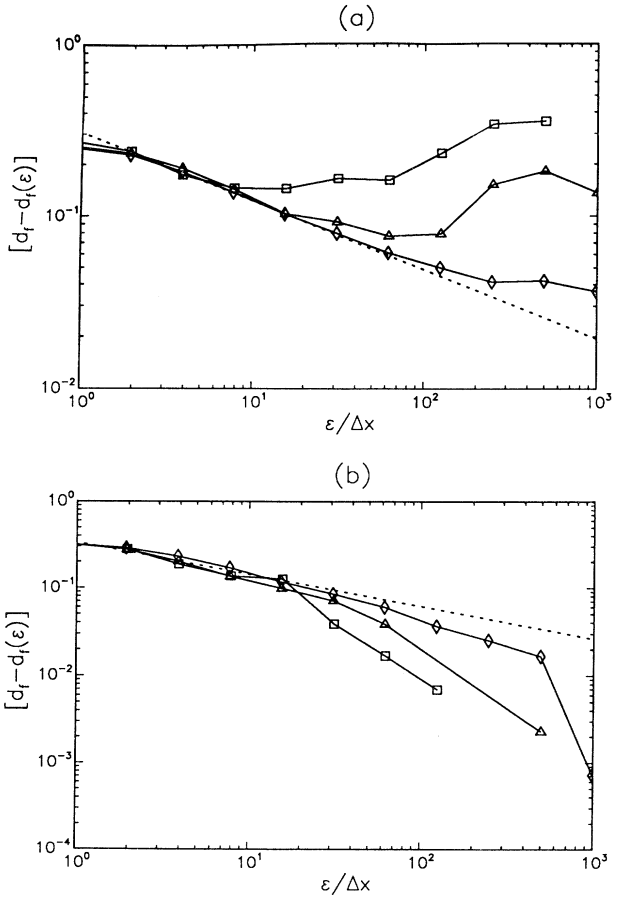

FIG. 7. Analysis of the scaling correction in the middle scale range for the Weierstrass and the FIT functions at different resolutions. Squares, $\Delta x = 2^{-10}$; triangles, $\Delta x = 2^{-12}$; diamonds, $\Delta x = 2^{-16}$. (a) $[1.6 - d_f(\varepsilon)]$ vs $\varepsilon/\Delta x$ for the Weierstrass function. The slope of the dotted line is -0.4. (b) $[1.63 - d_f(\varepsilon)]$ vs $\varepsilon/\Delta x$ for the FIT function. The slope of the dotted line is -0.37.

The problem is that all these methods assume that the information provided by $N_m(\varepsilon)$ about the behavior on scale ε is realistic. Yet, as we have seen, this is generally not correct. We can better understand this point if we compare the evaluation of $N_m(\varepsilon)$ with the computation of the power spectrum $E[k]$, which also carries information about the behavior on scale $\varepsilon \sim 1/k$. The finer the resolution, the higher the number of Fourier frequencies that can be computed via a fast Fourier transform. But the resolution influences only the number of Fourier components that can be calculated, not the precision with which a single component is known. Instead, the accuracy with which $N(\varepsilon)$ is known depends on the number of scales below ε that are actually resolved. The reason is that the local fractal dimension is related to the measure of the graph on that scale, a notion that involves the knowledge of all the points that make up the graph. Moreover, in dealing with real turbulent signals, we have to keep in mind that the self-affine behavior is expected to cease above the integral scale l, and also that below the Kolmogorov scale η_k a turbulent signal becomes smooth because of the action of viscosity (in this respect, a turbulent signal is intrinsically a prefractal). Therefore, we expect significant scaling corrections of the kind we have considered in Sec. IV C for scales below $10^3\eta_K$. In particular the scaling can be modified over the entire range if the ratio $l/\eta_K < 10^3$. The same considerations apply if we filter the signal. In this case the Kolmogorov scale is replaced by the inverse of the filtering frequency. In practice, it thus becomes necessary to infer the fractal nature and dimension from a suitable combination of leading scaling and scaling correction. As we have seen, the correction to the scaling of a prefractal has specific features that can be thought as a sort of "fractal signature." These are (i) the exponential approach of $d_f(\varepsilon) - d_f$ to zero with half time $(2 - d_f)^{-1}$ in the intermediate scale range (if d_f is the correct value) and (ii) the log-linear behavior near the smallest resolved scales of the scaling correction $f(\varepsilon, \Delta x)$. These are features that can be checked in practice. In both cases one has to try several *Ansätze* for the leading scaling, until a self-consistent behavior is obtained. When this value is reasonably larger than one, we can conclude that the signal is indeed a prefractal. To systematically establish fractality and fractal dimension of a signal, we propose the following general guidelines.

(i) In order to obtain a first estimate of the dimension, evaluate the fractal dimension from the power spectrum's decay exponent α according to $d_f^* = (5 - \alpha)/2$. If the process is known to be multipoint Gaussian, then $d_f = d_f^*$.

(ii) Measure the local fractal dimension $d_f(\varepsilon)$.

(iii) Check if the scaling correction (at least in some ranges) is consistent with the assumed fractal dimension

TABLE I. Experimental parameters of data sets. f_s is the sampling frequency, f_p the cutoff frequency, η_K the Kolmogorov scale, and η_c the cutoff scale. Pairs with and without the asterisk denote values for bands 1 and 2, respectively.

Parameter	Flow			
	BLL	CYL	BLH	ATM
$\mathrm{Re}=U_{\mathrm{mean}}L/\nu$	6.75×10^5	10^5	3.6×10^6	$\sim7\times10^6$
L (m)	~1.1	0.05	~1.1	~18
U_{mean} (m/s)	9.2	27.3	49.1	~6
η_K (cm)	0.054	~0.01	0.015	~0.07
f_s (kHz)	0.8, 80*	60	4, 80*	6
f_p (kHz)	0.2, 20*	30	1, 20*	2
$\eta_c=U_{\mathrm{mean}}/f_p$ (cm)	4.5, 0.045*	0.091	4.32, 0.22*	0.3
Number of points for each record	2^{12}	2^{13}	2^{12}	2^{16}
Total number of records	100	100	100	4

d_f^*. This amounts to verifying that Eqs. (22) and (24) are satisfied with $d_f=d_f^*$.

(iv) If the slope is the one expected and this happens in a range of scales consistent with the analysis of the power spectrum, then we can conclude that the signal is prefractal and that the fractal dimension is $d_f=d_f^*$.

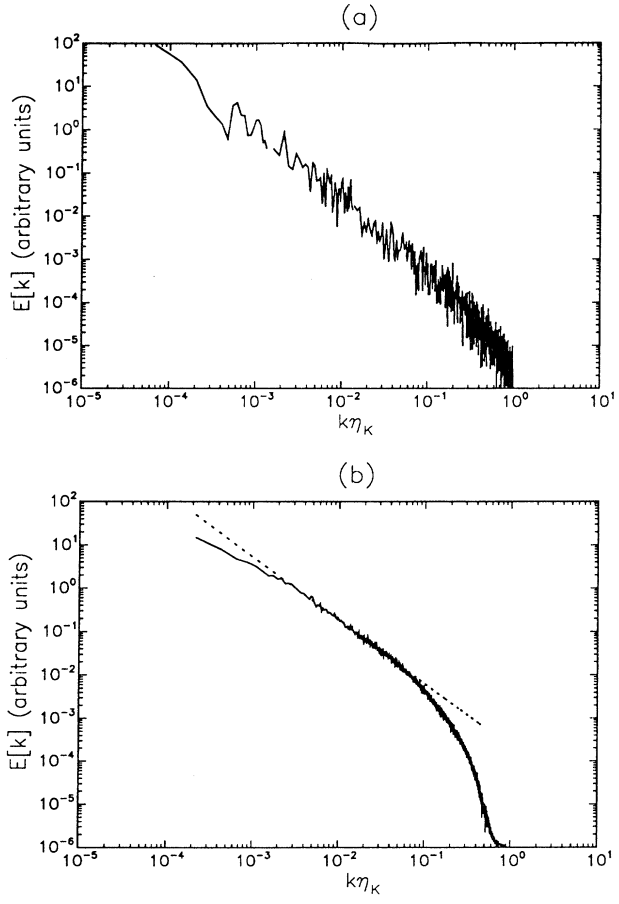

FIG. 8. Power spectra of (a) the atmospheric data and (b) cylinder wake data. The slope of the dotted line is -1.5.

(v) If not, repeat step (iii) with different values for d_f and see if Eqs. (22) and (24) are satisfied. If they are (with some $d_f\neq d_f^*$) we may conclude that the graph is prefractal, but that non-Gaussian statistics affect the relationship between α and d_f.

(vi) If Eqs. (22) and (24) cannot be satisfied with any reasonable $d_f>1$ value over any reasonable scale range, then the graph is not a prefractal.

V. DESCRIPTION OF DATA SETS

Hot-wire measurements taken in four types of turbulent flows have been analyzed. They are the turbulent wake past a cylinder (CYL), a low-speed turbulent boundary layer generated by a rough wall (BLL), a high-speed turbulent boundary layer generated by a rough wall, (BLH), and the turbulent atmospheric layer (ATM). Table I summarizes the experimental parameters for each data set.

A. Atmospheric surface layer (ATM)

These are the data strings with the largest scale ratio that we have analyzed. As the power spectrum shows [Fig. 8(a)], almost the entire data lies inside the inertial range. The spectrum follows a $-\frac{5}{3}$ law for more than two decades. Given the length of the strings and the good scaling of the power spectrum, we expect to be able to observe fractal scaling. However, due to the fact that this is a geophysical flow where significant large-scale variability existed, the length of the measurement is insufficient to yield well-converged statistics. More details about this data set are given in Ref. [3].

B. Cylinder wake (CYL)

These data were taken in the turbulent wake behind a cylinder. The experiment was performed in the Corrsin wind tunnel (see Ref. [25]). Only fluctuations of the streamwise component of velocity were recorded. The power spectrum is shown in Fig. 8(b). Since in this case the wire length exceeds the Kolmogorov scale, the value

of η_K given in Table I (computed as in Ref. [25]) is only approximate.

C. Boundary layer: Low-speed case (BLL)

These data were collected in the test section of the 80×120 ft^2 Full Scale Aerodynamic Facility at NASA Ames Research Center. Due to the size of this facility, it is possible to reach very high Reynolds numbers in a controlled fashion. Measurements were taken in the outer region of the boundary layer, at $y/\delta\sim0.9$, where δ is the boundary layer thickness ($\delta\sim1.1$ m). See Ref. [26] for a more detailed discussion of similar data taken at lower y/δ values. Fluctuations of the vertical as well as streamwise velocity component were measured. To enhance the bandwidth resolution for each component, data were taken in two different spectral bands, with different sampling frequencies and low-pass cutoff filters. In Fig. 9(a) the power spectrum of the two bands combined together is shown. The first band presents a good $-\frac{5}{3}$ scaling over about 1.5 decades, while the second one curves down after one decade. For this reason we have analyzed only the data in band 1.

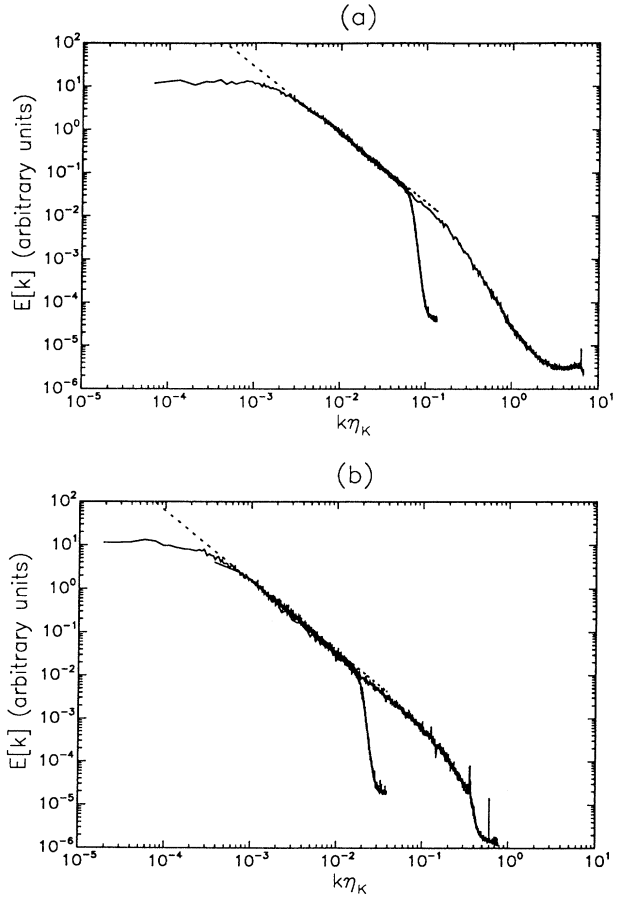

FIG. 9. Power spectra of (a) the low-speed boundary layer data in the streamwise direction and (b) the high-speed boundary layer data for the streamwise component for bands 1 and 2. The slope of the dotted line is -1.6 in both cases.

D. Boundary layer: high-speed case (BLH)

This is the second set of measurements taken in the NASA Ames facility, at a free stream velocity U_∞ of 50 m/s, at $y/\delta\sim0.8$. In this case the data have also been acquired in different bands, but using three bands, due to the longer inertial range. Table I contains the relevant flow parameter and sampling and cutoff frequencies. Only the first two bands have been considered, due to the presence of noise in the high-frequency region of the last band and spatial attenuation of the smallest scales due to the length of the wire (see Ref. [26]). In Fig. 9(b) the power spectrum of the two bands are combined together to give a global view. The $-\frac{5}{3}$ scaling is evident over more than two decades. For the second band we expect to find fractal scaling with possibly some scaling corrections due to the filtering. The first band lies in part outside of the inertial range, the part inside covering less than two decades.

Both the high- and the low-speed measurements were taken in the outer regions of the boundary layer, where "outer intermittency" was observed. Intermittent segments of the data sets exhibit low turbulence intensity, corresponding to outer fluid being engulfed into the boundary layer. This contributes to deviations from multipoint Gaussian statistics and thus serves as an interesting test to see if this causes differences between d_f^* and d_f.

VI. RESULTS

In this section, the experimental data sets are analyzed. For each segment of data, we compute $N_m(\varepsilon)$ and the local slope $d_f(\varepsilon)$ in the log-log plot. Then, averages are taken over 100 segments of data, except for the atmospheric case, where only 4 segments were available. With 100 segments of data, statistics are well converged. Error bars for $N_m(\varepsilon)$ and $d_f(\varepsilon)$ are generated by calculating the variance of $N_m(\varepsilon)$ and $d_f(\varepsilon)$ between segments of data. With the exception of the atmospheric layer data, the

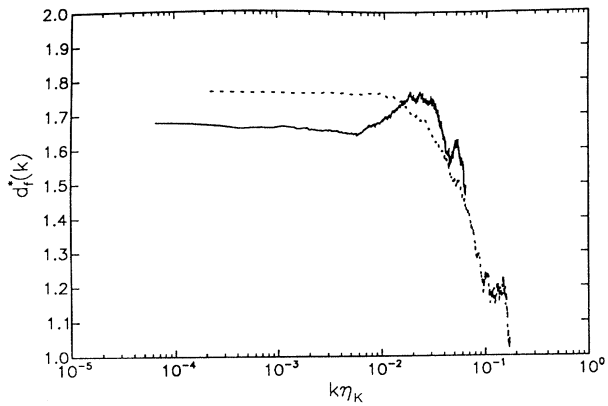

FIG. 10. Local fractal dimension $d_f^*(k)=[5-\alpha(k)]/2$ obtained from the local slope $\alpha(k)$ of the spectrum of the streamwise velocity component in the atmospheric layer (solid line) and in the wake of the cylinder (dashed line).

statistics can be regarded as converged. In the following subsections, we discuss the results for each flow separately.

A. Atmospheric turbulence

The ratio between the largest scale within the inertial range and the cutoff scale is about 3.5×10^4. Having just four strings of data, the spectrum $\langle\hat{u}(k)\hat{u}^*(k)\rangle$ is very noisy [see Fig. 8(a)]. The local spectral dimension $d_f^*(k)$ is shown in Fig. 10 (solid line), using a smoothing window that includes 1000 modes to compute the local slope. The plateau corresponds to $d_f^*=1.68$. In Fig. 11 we show the results of box counting (squares) and the variational method (triangles). The dashed line has been plotted only for comparison and shows the best linear fit that can be obtained by fixing the slope to $\frac{5}{3}$. As expected, for about one decade at the large scales, $d_f(\varepsilon)$ as given by box counting oscillates around 1.68. We have also applied the variational method in this case in order to check whether these oscillations are due to the discrete nature of box counting. The results show indeed a range where the $d_f(\varepsilon)=1.68$ (triangles in Fig. 11). Also noticeable is how the two methods agree at small scales. As a consistency check, we now consider the scaling corrections using the approach described in Sec. IV. We observe both the log-linear approach near the cutoff scale [Fig. 12(a), and 12(b), squares] and the exponential approach where the *Ansatz* $d_f=1.68$ is used [Figs. 13(a) and 13(b), squares].

B. Cylinder wake

The circles in Fig. 11(b) show the results of box counting as applied to the cylinder data. The flattening of the local dimension at large scales seems to suggest the value of 1.75 for the global dimension. Figure 12 (circles) shows the log-linear behavior of $f(\varepsilon,\Delta x)$ when $d_f=1.75$ is used for the leading scaling. The middle range exponential approach (Fig. 13, circles) also confirms that 1.75 is a good estimate. The flattening of the spectrum at large scales ($d_f^*=1.75$) (see Fig. 10, dashed line) also suggests that this is a realistic value.

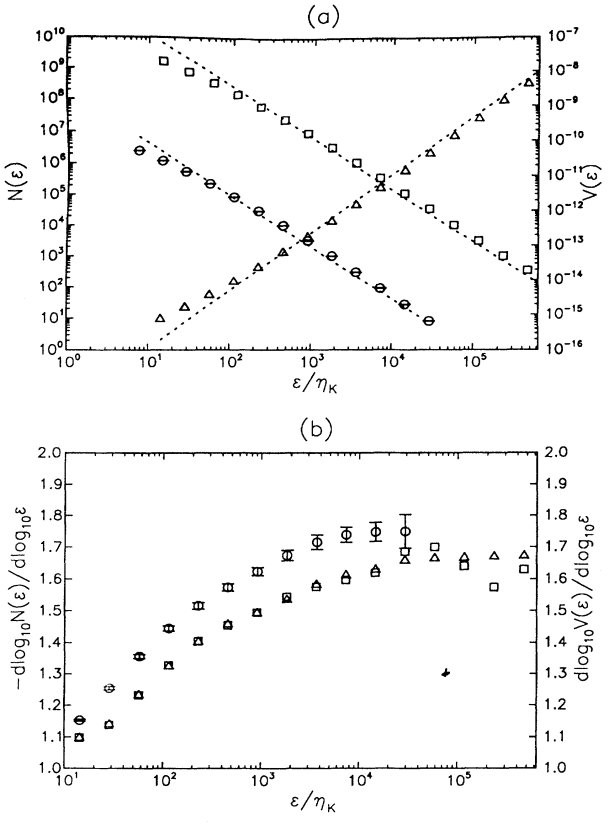

FIG. 11. Box counting and variational method applied to the atmospheric surface layer (ATM) and cylinder wake (CYL) data. (a) Box counting for CYL (circles), box counting (squares) and the variational method (triangles) for ATM; the dotted lines mark the expected value for the slope $d_f=1.66$. (b) Local slope obtained from (a); the symbols are the same as in (a).

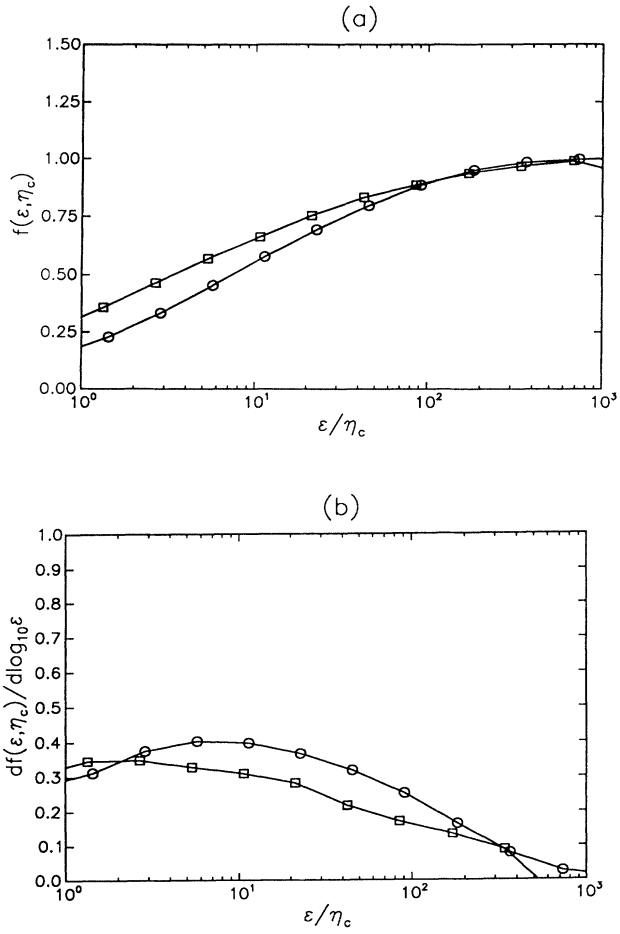

FIG. 12. Scaling correction at small scales for ATM and CYL. (a) $f(\varepsilon,\eta_c)$ vs $\log_{10}\varepsilon/\eta_c$: squares correspond to ATM calculated with a leading exponent $d_f=1.68$, while circles correspond to CYL with $d_f=1.75$. (b) Local slope of (a) vs ε/η_c.

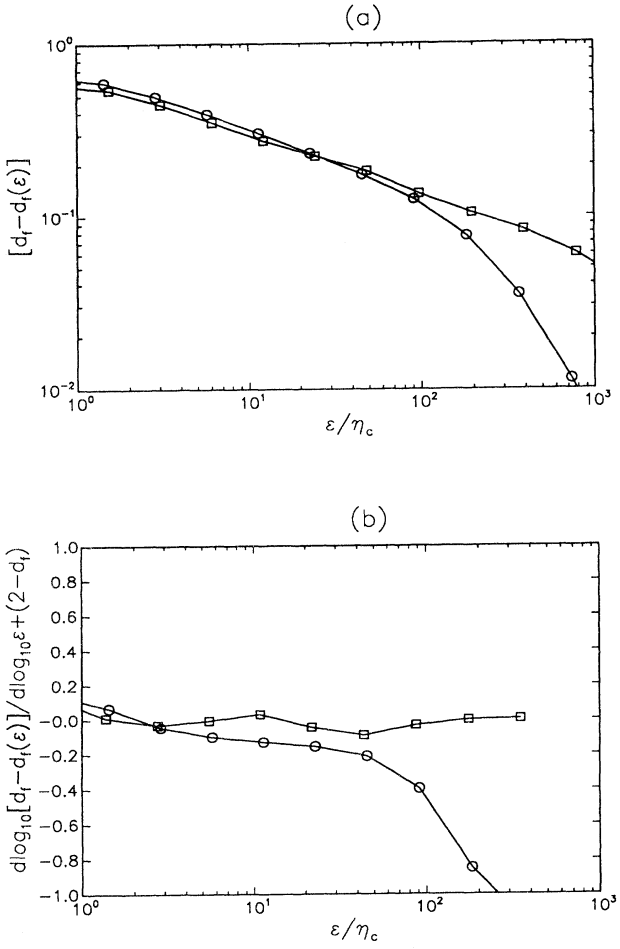

FIG. 13. Scaling correction in the middle scale range for the ATM and the CYL data: (a) $[d_f-d_f(\varepsilon)]$ vs ε/η_c for ATM with $d_f=1.68$ (squares) and for CYL with $d_f=1.75$ (circles). (b) $d\log[d_f-d_f(\varepsilon)]/d\log(\varepsilon/\eta_c)+(2-d_f)$ vs ε/η_c, same symbols as in (a).

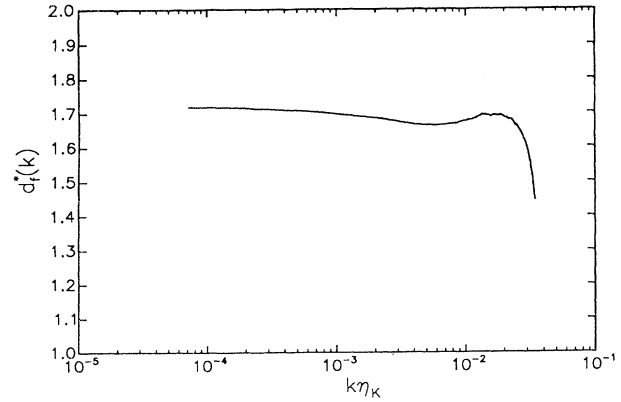

FIG. 14. Local fractal dimension $d_f^*(k)=[5-\alpha(k)]/2$ obtained from the local slope $\alpha(k)$ of spectrum of the streamwise component in the low-speed boundary layer.

C. Boundary layer: low speed

1. Streamwise component

Figure 14 shows the dimension computed from the slope of the spectrum. In this case we conclude that $d_f^*=1.7$. Figure 15(b) (squares) shows that for this signal the local fractal dimension remains always below 1.66. However, a closer look at the scaling corrections [Figs. 16(a), 16(b), and 17(b) and 17(b) squares] shows that d_f is probably closer to 1.7. Indeed, the best log-linear fitting is achieved for $d_f=1.7$ as seen in Fig. 16 (squares). Using the same value, the exponential approach in the middle range is followed for two decades remarkably well [Figs. 17(a) and 17(b), squares].

2. Vertical component

Here the local dimension reaches the maximum value of 1.66 and eventually curves down, although 1.66 remains within the range of the error bars [Fig. 15(b), cir-

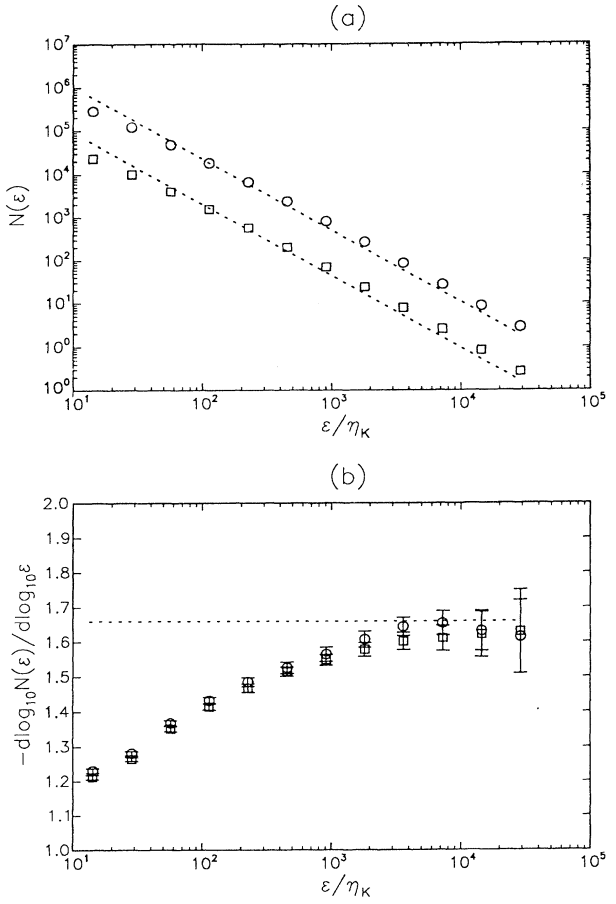

FIG. 15. Box counting applied to the low-speed boundary layer data. Circles correspond to the vertical component and squares to the streamwise velocity component. Error bars refer to the standard deviation evaluated over 100 records. (a) $N_m(\varepsilon)$ vs ε/η_K (the vertical component is offset for clarity). (b) Local fractal dimension. The dashed line shows $d_f=\frac{5}{3}$.

cles]. Figure 16 (circles) shows the small-scale limit of $f(\varepsilon,\Delta x)$, using as leading scaling the value 1.7. The log-linear behavior is not fully reproduced in this case. The best exponential approach is achieved when d_f is set equal to 1.68 [Figs. 17(a) and 17(b), circles], even though the range of scales over which the exponential approach is observed is smaller than for the streamwise component.

The fact that slightly different values of d_f are obtained depending on the criterion we use is not surprising, especially considering that the relative dispersion of these figures is well within the average value of the standard deviation of the local fractal dimension.

D. Boundary layer: High speed

As pointed out before, the data analyzed consist of two bands. Since band 1 lies partly outside of the inertial range at the outer scale, we expect that the large-scale behavior of the local dimension will not reflect the actual value of d_f.

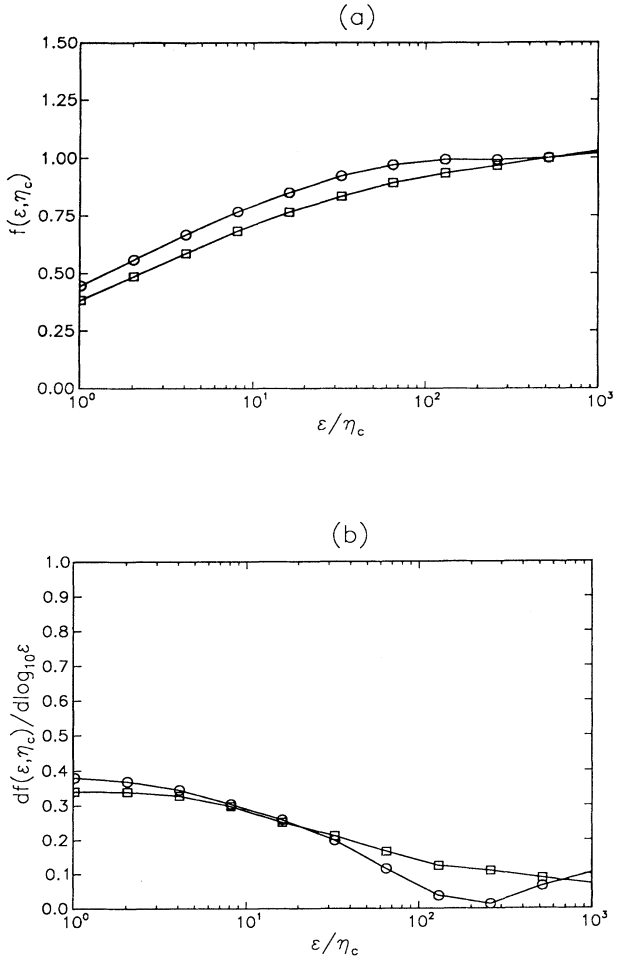

FIG. 16. Scaling correction at small scales for the low-speed boundary layer: (a) $f(\varepsilon,\eta_c)$ vs ε/η_c calculated with the leading exponent $d_f=1.7$ for both the streamwise (squares) and the vertical (circles) component. (b) Local slope of (a) vs ε/η_c.

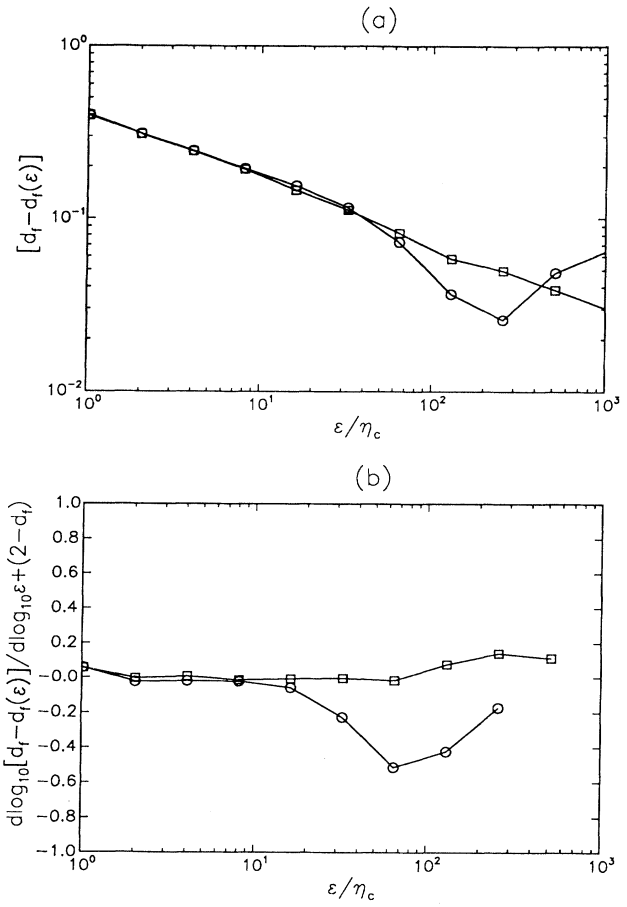

FIG. 17. Scaling correction in the middle scale range for the low-speed boundary layer. Circles correspond to the vertical component with $d_f=1.68$ and squares correspond to the streamwise component with $d_f=1.7$. (a) $[d_f-d_f(\varepsilon)]$ vs ε/η_c. (b) $d\log_{10}[d_f-d_f(\varepsilon)]/d\log_{10}(\varepsilon/\eta_c)+(2-d_f)$ vs ε/η_c.

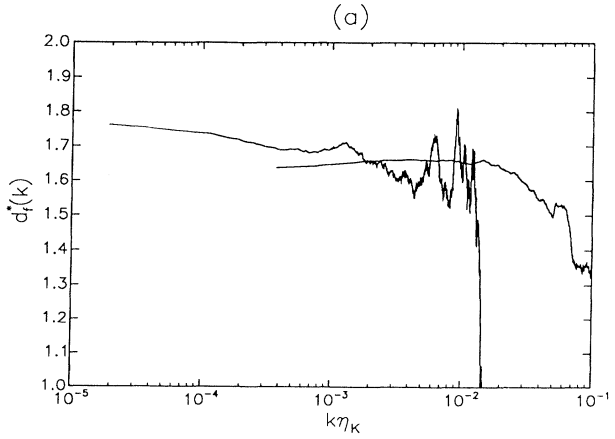

FIG. 18. Local fractal dimension $d_f^*(k)=[5-\alpha(k)]/2$ obtained from the local slope $\alpha(k)$ of spectrum of the streamwise component in the high-speed boundary layer.

1. Streamwise component

Figure 18 shows the dimension as calculated from the slope of the spectrum. The resulting values for d_f^* are 1.65 and 1.7 for bands 2 and 1, respectively. These estimates are apparently contradicted by the analysis of the local dimension, which seems to tend to 1.75 and 1.5 at large scales, [Figs. 19(a) and 19(b), squares and triangles]. However, for band 1 the best results are achieved if one uses 1.66 as the leading scaling for the log-linear behavior at small scales (Fig. 20, triangles), while the exponential approach at larger scales is reached if d_f is set to 1.68 (Fig. 21, triangles). For band 2, the small-scale limit of $f(\varepsilon,\Delta x)$ computed with a leading scaling equal to 1.66 shows a fair log-linear approach (Fig. 20, squares), while to achieve a good exponential approach in the middle range the value of 1.68 is preferable.

2. Vertical component

The analysis of the first band gives results similar to the one observed for the streamwise component. The dimension inferred from the slope of the spectrum is 1.65.

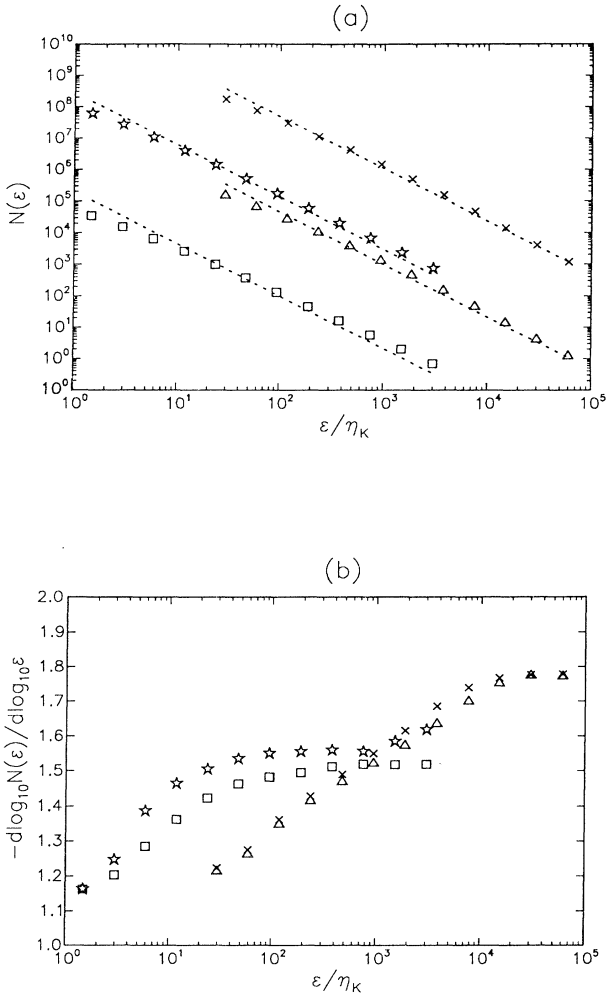

FIG. 19. Box counting applied to the high-speed boundary layer data. Squares and triangles corresponds to bands 2 and 1 of the streamwise component, respectively. Stars and crosses correspond to bands 2 and 1 of the vertical velocity component, respectively. The dashed line shows $d_f = \frac{5}{3}$. The standard deviation of the local slope, not reproduced for clarity, is about 5%. (a) $N_m(\varepsilon)$ vs ε/η_K (the vertical component is offset for clarity). (b) Local fractal dimension.

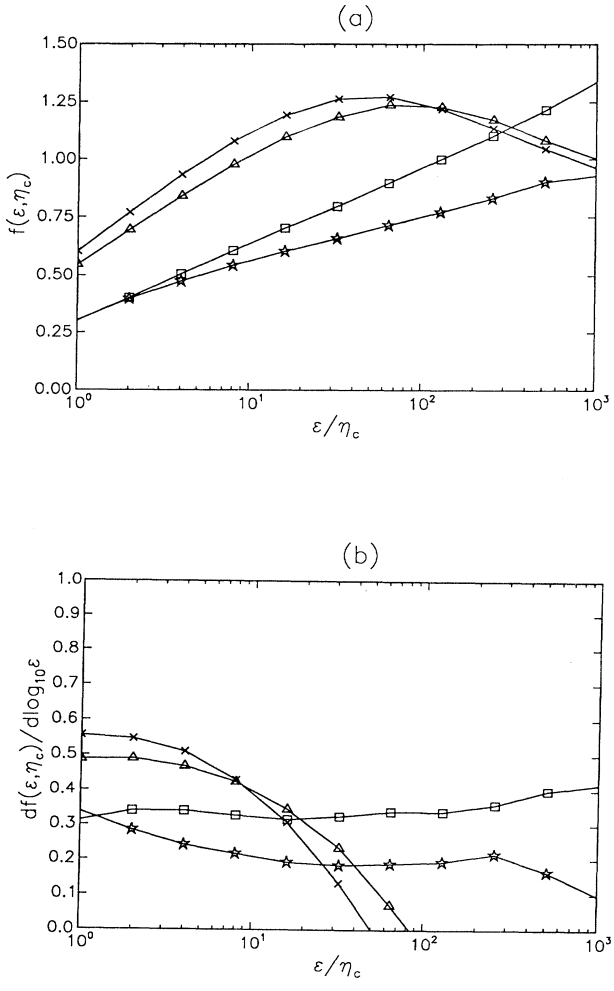

FIG. 20. Small-scale log-linear behavior for the high-speed boundary layer data. Squares and triangles correspond to bands 2 and 1 of the streamwise component with $d_f = 1.66$ and 1.7, respectively. Stars and crosses correspond to bands 2 and 1 of the vertical component with $d_f = 1.66$ and 1.7, respectively. (a) Scaling correction $f(\varepsilon,\eta_c)$ vs ε/η_c calculated with leading exponent d_f. (b) Slope of (a) vs ε/η_c.

TABLE II. Summary of measured fractal dimensions of turbulent velocity signals. U denotes the streamwise component and V the vertical component.

	Flow							
	BLL		CYL	BLH				ATM
Band	1	1		1	1	2	2	
Component	U	V	U	U	V	U	V	U
d_f^* spectrum	1.7	1.65	1.75	1.65	1.7	1.65	1.7	1.68
d_f small	1.7	1.7	1.75	1.66	1.66	1.66	1.66	1.68
d_f middle	1.7	1.68	1.75	1.68	1.68	1.68	1.68	1.68

Figure 19 (crosses) shows the results from box counting. The leading exponent that best achieves the expected log-linear profile at small scale is 1.66 [Figs. 20(a) and 20(b) crosses], while using for d_f the value of 1.68 we achieve a good exponential approach in the middle range, as Figs. 21(a) and 21(b) (crosses) show. For the second band the analysis of the spectrum seems to suggest for d_f the value 1.7. At small scales the log-linear behavior is achieved setting the leading exponent to 1.66 (Fig. 20(a),(b) stars), whereas the leading scaling for which the half life is closest to the expected value is 1.68 [Figs. 21(a) and 21(b)], although it is not very extensive.

Table II summarizes the main results.

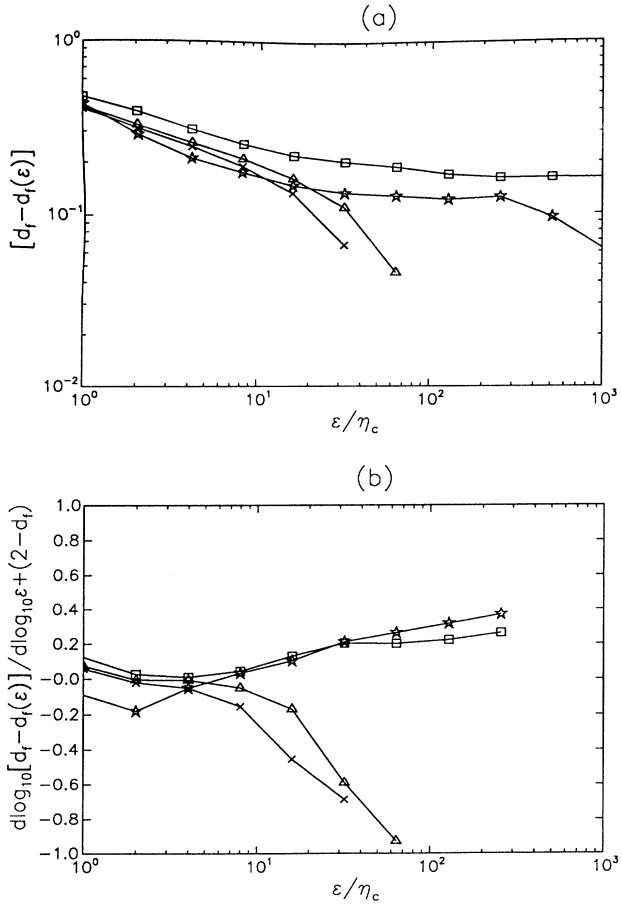

FIG. 21. Scaling correction in the middle scale range for the high-speed boundary layer data. Squares and triangles correspond to bands 2 and 1 of the streamwise component with $d_f = 1.68$ and 1.68, respectively, while stars and crosses correspond to bands 2 and 1 of the vertical component with $d_f = 1.68$ and 1.7, respectively. (a) $[d_f - d_f(\varepsilon)]$ vs ε/η_c. (b) $d\log_{10}[d_f - d_f(\varepsilon)]/d\log_{10}(\varepsilon/\eta_c) + (2 - d_f)$ vs ε/η_c.

VII. SUMMARY AND CONCLUSIONS

In this paper the fractal nature of velocity signals in turbulent flows has been studied. An attempt was made to test for fractality by taking logarithmic derivatives, but several calibration experiments with signals of known fractal dimension proved that finite-size effects had to be taken into account explicitly. The effort spent in these calibration experiments was rewarded by the finding that the corrections have a general form. More important, we found that these corrections carry information about the global fractal dimension and this fact can be exploited to measure this dimension. This result may be quite general and may find applications to fractal analysis in other contexts. When applied to turbulence data, the proposed data analysis procedure shows that turbulent velocity signals are indeed prefractals By this we mean to say that the signals respond to our method of analysis in a way that is consistent with our predictions. As far as the fractal dimension is concerned, we found that most of the data and methods give a value around $d_f = 1.7 \pm 0.05$ and some data at lower Reynolds number gave $d_f \sim 1.75$. These results are quite consistent with Orey's theorem for Gaussian processes, as well as with previous results [14] in which turbulence data was shown to follow Orey's theorem. With this more detailed analysis of the scaling correction, we conclude that the non-Gaussian nature of turbulence does not significantly modify the relation between the spectral exponent and the fractal dimension of the graph of velocity.

ACKNOWLEDGMENTS

A.S. acknowledges support from CNR, Grant No. N.203.01.60. C.M. and A.S. acknowledge partial support from NSF, Grant No. CTS-9113048. S.G.S. would like to thank the staff of the Full-Scale Aerodynamics Research Division at NASA for their cooperation.

[1] B. B. Mandelbrot, J. Fluid Mech. **62**, 331 (1974); **62**, 358 (1974).
[2] K. R. Sreenivasan, Annu. Rev. Fluid Mech. **23**, 539 (1991).
[3] C. Meneveau and K. R. Sreenivasan, J. Fluid Mech. **224**, 429 (1991).
[4] J. C. Vassilicos and J. R. C. Hunt, Proc. R. Soc. London Ser. A **435**, 505 (1991).
[5] I. Procaccia, A. Brandenburg, M. H. Jensen, and A. Vincent, Europhys. Lett. **19**, 183 (1992).
[6] R. R. Prasad, C. Meneveau, and K. R. Sreenivasan, Phys. Rev. Lett. **61**, 74 (1988).
[7] A. A. Praskovsky, W. F. Dabberdt, E. A. Praskovskaya, W. G. Hoydysh, and O. Holynskyj (unpublished).
[8] A. N. Kolmogorov, C. R. Acad. Sci. U.S.S.R. **30**, 301 (1941).
[9] A. Monin and A. Yaglom, *Statistical Fluid Mechanics* (MIT Press, Cambridge, MA, 1975).
[10] S. Orey, Z. Wahrscheinlichkeitstheorie Verw. Geb. **15**, 249 (1970).
[11] T. Higuchi, Physica D **46**, 254 (1990).
[12] J. Feder, Fractals (Plenum, New York, 1988).
[13] B. Dubuc, J. F. Quiniou, C. Roques-Carmes, C. Tricot, and S. W. Zucker, Phys. Rev. A **39**, 1500 (1989).
[14] K. R. Sreenivasan and A. Juneja (unpublished).
[15] A. A. Praskovsky, J. F. Foss, S. J. Kleis, and M. Y. Karyakin, Phys. Fluids A **5**, 2038 (1993).
[16] H. E. Schepers, J. H. G. M. van Beek, and J. B. Bassingthwaighte, IEEE Eng. Med. Biol. **11** (2), 57 (1992).
[17] B. B. Mandelbrot, in *Fractals in Physics,* edited by L. Pietronero and E. Tosatti (Elsevier Science, New York, 1986).
[18] R. F. Voss, Physica D **38**, 362 (1989).
[19] P. L. Miller and P. E. Dimotakis, Phys. Fluids A **3**, 168 (1991); **3**, 177 (1991).
[20] B. B. Mandelbrot, *Fractals: Form, Chance, and Dimension* (Freeman, San Francisco, 1977).
[21] M. V. Berry and Z. V. Lewis, Proc. R. Soc. London Ser. A **370**, 459 (1980).
[22] O. I. Yordanov and N. I. Nickolaev, Phys. Rev. E **49**, R2517 (1994).
[23] M. F. Barnsley, Constr. Approx. **2**, 303 (1986).
[24] M. F. Barnsley, *Fractals Everywhere* (Academic, Boston, 1988).
[25] J. O'Neil and C. Meneveau, Phys. Fluids A **5**, 158 (1993).
[26] S. G. Saddoughi and S. V. Veeravalli, J. Fluid Mech. **268**, 333 (1994).